Volume-conservative modeling of structures manufactured by molten drop-on-drop deposition

Rosendo Zamora [a], Félix Faura [a], Julio Hernández [b], Joaquín López [a],*

[a] *Dept. de Ingeniería Mecánica, Materiales y Fabricación, ETSII, Universidad Politécnica de Cartagena, E-30202 Cartagena, Spain*
[b] *Dept. de Mecánica, ETSII, UNED, E-28040 Madrid, Spain*

HIGHLIGHTS

- The new analytic model improves the geometry prediction of manufactured structures.
- The model exactly conserves the volume of the deposited material.
- The model preserves the contact angle between consecutive deposited droplets.
- Good degree of agreement between theoretical and experimental results is achieved.

GRAPHICAL ABSTRACT
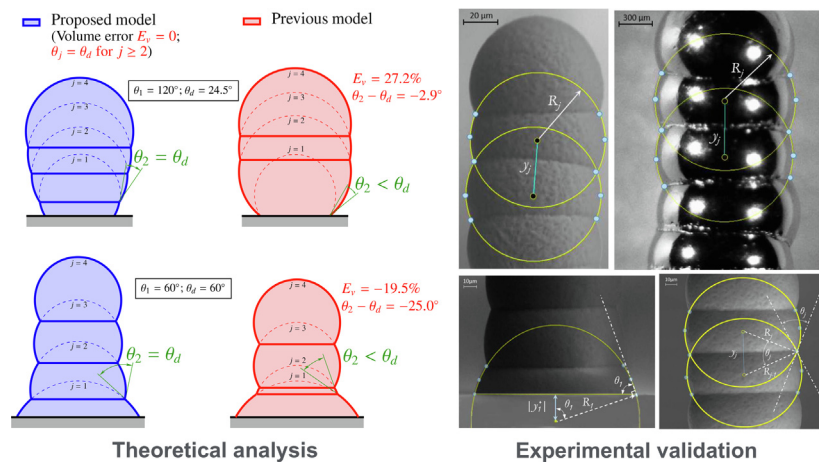
ABSTRACT

An improved analytic model to accurately determine the geometry of structures manufactured by molten drop-on-drop deposition is presented. This deposition mode allows quasi-spherical deposited droplets to be achieved and precise control over the geometry of the final manufactured structures. The model exactly conserves the volume of the deposited material and matches the solidification contact angle between consecutive deposited droplets, providing a precise geometrical description of the manufactured structures. The proposed model is validated using results of experiments performed with several materials for the deposited droplets and substrate, and droplet radii ranging from 40 to 800 μm. A good degree of agreement was found between theoretical and experimental results. A comparison with the well-established Gao&Sonin model shows that the proposed model represents a major improvement, and may be of great practical interest in industrial applications.

© 2022 The Author(s). Published by Elsevier Ltd. This is an open access article under the CC BY-NC-ND license (http://creativecommons.org/licenses/by-nc-nd/4.0/).

1. Introduction

Additive manufacturing by molten droplet deposition has been attracting much interest in recent years due to the digital nature of the process, which allows high dimensional accuracy of the manufactured part to be achieved through the precise control of droplet

* Corresponding author.
  E-mail address: joaquin.lopez@upct.es (J. López).

deposition. A great deal of effort is currently being devoted to understanding the complex phenomena involved in the deposition process. One of the pioneer works on this subject was carried out by Gao and Sonin [1], who studied, both theoretically and experimentally, the dynamic and thermal aspects under some basic modes of precise deposition and solidification of molten droplets, and discussed the conditions required for controlled deposition. These basic models include (1) drop-on-drop deposition to manufacture pillars, (2) sweep deposition to manufacture continuous beads on flat surfaces and (3) a combination of both to manufacture larger parts.

Another additive manufacturing process capable of producing pillars is, for example, laser powder bed fusion [2]. In addition to additive manufacturing, these pillars can also be produced by high-speed electrodeposition [3], sinter molding [4], or micro-machining [5,6]. Micro-machining can produce micro-pillars with very close dimensional tolerances and very good surface finishes. However, the size of the cutting tools and the forces acting on the pillars during the cutting process severely limit the minimum distance between pillars and the maximum aspect ratio between pillar height and diameter. In general, the main advantages of additive manufacturing by molten droplet deposition compared to the other processes mentioned above are the less expensive equipment requirements, the greater flexibility to create structures of high geometric complexity, and the ability to easily produce multi-material objects.

The present work focuses on additive manufacturing by drop-on-drop deposition. Fig. 1 shows two examples of structures that can be manufactured using this deposition mode (the column on the left is completely aligned with the deposition direction, while the one on the right is not). There are many industrial applications using the drop-on-drop mode, for which the accuracy in the geometry of the manufactured structure is a crucial factor. Examples, among others (see, e.g., a recent review in [7]), include chip-scale packaging [8], solder towers suitable for electrical interconnects [9], manufacturing of precise metallic micro-components [10,11], manufacturing of multi-metal components [12], micro-manufacturing of structures using high melting temperature metals using a laser-based drop deposition technique [13]or a magnetohydrodynamic jetting technique [14], manufacturing of structures using precious metals for advanced electronic components [15], manufacturing of jewelry [16], and manufacturing of wereable biosensors [17], bioactive coatings on implant materials [18], and three-dimensional microarchitectural materials and devices for a wide range of applications [19]. The size and number of droplets required to build these structures depend on multiple factors, such as their functionality or performance. For example, one can find from sub-millimeter-sized connections that require depositing only a few drops [20], to thin-walled metallic parts with a size of several millimeters that require depositing dozens of drops [21].

The influence of several operating conditions on the thermo-fluid dynamics of the different phenomena involved during the drop-on-drop deposition process to manufacture vertical metallic columns has been investigated by several authors. Among these operating conditions, the droplet temperature, substrate temperature and deposition frequency, were studied experimentally by Fang et al. [22] for tin or by Fang et al. [23] for an aluminum alloy, while the distance from nozzle to substrate and the impact velocity of the molten droplets against the substrate were investigated by Wang et al. [24]. Other detailed studies of the transient transport phenomena that occur during the deposition and solidification of multiple metal droplets over a static substrate to form micro-columns were carried out numerically by Che et al. [25], and both numerically and experimentally by Haferl and Poulikakos [26,27], Gilani et al. [12] and Liu et al. [28].

The first analytic model to predict the final shape of structures manufactured by drop-on-drop deposition was proposed by Gao and Sonin [1]. They provided analytic relationships to estimate the geometry of manufactured structures and to determine the cooling and solidification times of deposited droplets. Based on this model (Gao&Sonin model), authors like Chao [10] or Zhang et al. [29], among others, estimate the geometry of structures manufactured by drop-on-drop deposition and, recently, Zhang et al. [30] performed a parametric mapping of the morphology of structures manufactured under this deposition mode for different spacings between consecutive deposited droplets (a discussion on the errors in the deposition location and their influence on the manufactured structure can also be found in [30]). However, none of these calculations rigorously preserves the volume of the deposited material or coincides with the solidification contact angle between consecutive deposited droplets, which makes it difficult to obtain accurate predictions of manufactured structures under certain operating conditions. In this work, a new conservative analytic model that avoids the above limitations is proposed and several experiments are performed for its validation. The improvement achieved with the proposed model may represent an important advance in the prediction of the final-shape of structures manufactured by droplet deposition under the operating conditions considered in this work, and therefore be of great help in process planning and manufacturing automation.

2. Problem statement

Let us consider the manufacturing of columns by drop-on-drop deposition of n molten droplets with initial radius R_{in}. The analytic model proposed in this work is based on the following assumptions:
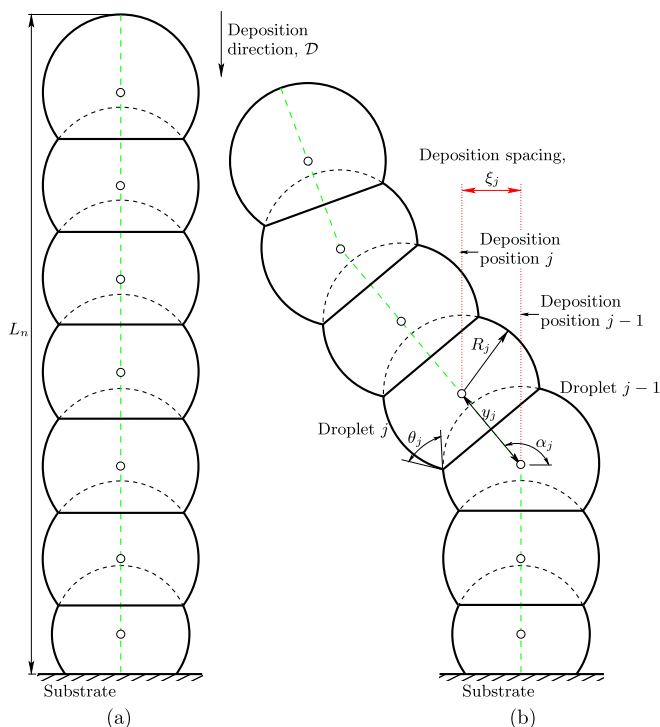

Fig. 1. Examples of two columns of $n = 7$ droplets manufactured by drop-on-drop deposition. (a) Zero and (b) non-zero droplet deposition spacing, ξ_j.

- During the impact and spreading of molten droplets, capillary forces dominate over the inertial effects, causing the deposited molten droplets to rapidly reach a spherical shape.
- The frequency of droplet deposition is assumed to be sufficiently low, so that a pre-deposited droplet solidifies completely before a new incoming molten droplet is deposited on it. High values of the deposition frequency may produce an excess of input energy, causing an incoming droplet to hit a previous one that is still in a mushy state. Good examples illustrating the importance to taking this consideration into account can be seen, for example, from the numerical results presented in [28](Fig. 11 and others) or from the experimental results presented in [22], where the mass of liquid that accumulates at the tip of the column when using an excessively high deposition frequency can lead to significant failures in the manufactured pillar.
- The impact and inertial-capillarity time scales are assumed to be considerably lower than the solidification time scale.
- The net volume change after solidification and cooling of the deposited droplet is assumed to be negligible.

Under operating conditions close to the above assumptions, it is expected that the deposited droplets tend to reach solidified spherical shapes, allowing precise control of the deposition process and a good prediction of the final shape of the manufactured structures. This low-frequency deposition mode was named by Gao and Sonin [1] as dropwise mode. In addition, the following assumptions will be made:

- The centers of the spheres fitted to the deposited droplets (marked with ∘ symbols in Fig. 1) do not deviate from their corresponding deposition location (marked with red dotted lines in the example on the right of Fig. 1). From the experimental observations made by Gao and Sonin [1], this assumption is sufficiently justified if the inertial effects are insignificant compared to the capillary forces, as is the case for the conditions considered in this work. It should be noted that there may be practical situations with poor metallurgical bonding between neighboring droplets, caused, for example, by inappropriate heat accumulation effects or by molten metal oxidation phenomena, in which the above assumption may not be satisfied. To avoid these situations, the deposition frequency should be properly controlled to get a correct heat accumulation at the tip of the column that promotes good bonding between thee droplets; in addition, the molten metal droplets should be isolated, as much as possible, from the ambient air to prevent oxidation. An analysis of these situations will be reported elsewhere.
- The model will be applicable for any arbitrary angle formed between the deposition direction and the substrate.

Let us consider index j to denote the order in which a droplet is deposited to build the structure. For $j = 1$, index $j - 1 = 0$ refers to the substrate, which in this work will be considered as a planar surface perpendicular to the direction $\mathscr{D}$ of droplet deposition. Based on the above assumptions, the following four parameters have been used to define the geometry of the manufactured structures:

1. The radius R_j of the sphere fitted to each deposited droplet, j, depends on the radius R_{in} of the incoming droplet, the radius R_{j-1} of the sphere fitted to the previously deposited droplet, $j - 1$, and the solidification contact angle, θ_j, between the deposited droplets j and $j - 1$ (hereafter, the solidification contact angle is simply referred to as contact angle for brevity).

2. The length y_j of the segment joining the centers of the spheres fitted to the deposited droplets j and $j - 1$ also depends on the same parameters mentioned in the previous point.

3. The angle α_j, formed by the segment of length y_j and the perpendicular to the deposition direction, $\mathscr{D}$, can easily be obtained from y_j and the spacing, ξ_j, between the droplet deposition location of j and $j - 1$ (see the picture on the right of Fig. 1). The spacing ξ_j results from the relative movement between the droplet generator and the substrate during the deposition of the droplets and will be defined with positive or negative signs if the droplet movement with respect to the substrate is made to the right or left, respectively.

4. The total length, L_n, of the manufactured structure (length of the dashed green lines in the structures depicted in Fig. 1) can be estimated from the sum of individual lengths y_j of the deposited droplets, from $j = 2$ to n, the distance y_1^+ from the substrate to the center of the sphere fitted to the first deposited droplet, and the radius R_n of the sphere fitted to the last deposited droplet.

3. Gao&Sonin model

This section briefly describes the well-stablished and widely used model proposed by Gao and Sonin [1].

3.1. First deposited droplet

A molten droplet with incoming radius R_{in} is deposited along the direction $\mathscr{D}$ on a flat substrate ($j = 1$). The contact angle defined by the interface of the first solidified deposited droplet and the substrate will be denoted as θ_1. The distance y_1^+ from the substrate to the center of the sphere fitted to the first deposited droplet is (see Fig. 2)

$$y_1^+ = R_1 \sin\left(\theta_1 - \frac{\pi}{2}\right), \tag{1}$$

where the radius R_1 of the sphere fitted to the first deposited droplet can be obtained from the following volume conservation constraint:
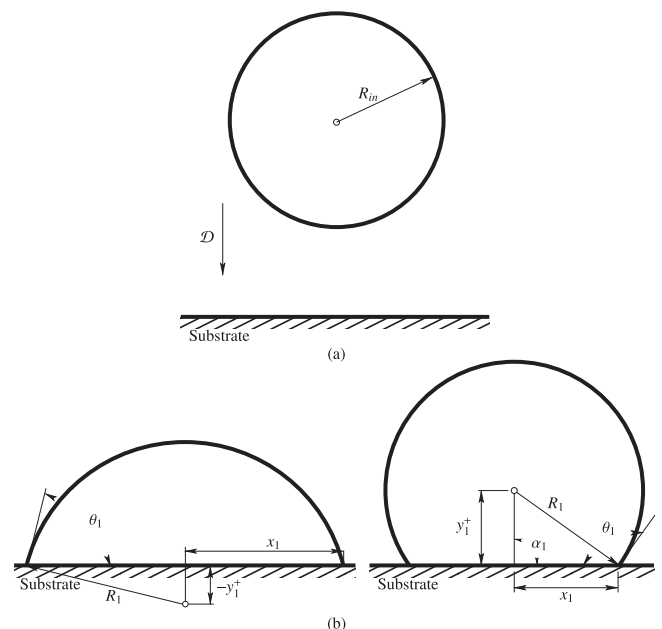

Fig. 2. First deposited droplet. (a) Before and (b) after deposition (left picture, $\theta_1 < \frac{\pi}{2}$; right picture, $\theta_1 > \frac{\pi}{2}$).

$$\frac{4}{3}\pi R_{in}^3 = \frac{4}{3}\pi R_1^3 - \frac{\pi}{6}\left(R_1 - y_1^+\right)\left[3x_1^2 + \left(R_1 - y_1^+\right)^2\right], \quad (2)$$

where the first term on the right is the volume of the sphere fitted to the deposited droplet, the last term represents the volume of the cap resulting from the intersection between the substrate and the fitted sphere, and

$$x_1 = R_1 \cos\left(\theta_1 - \frac{\pi}{2}\right), \quad (3)$$

is the semi-length of the intersection cap (see Fig. 2).

Introducing Eqs. (1) and (3) into Eq. (2) and arranging terms, yields

$$R_1 = \frac{R_{in}}{\gamma_1}, \quad (4)$$

and

$$y_1^+ = \frac{R_{in}}{\gamma_1}\sin\left(\theta_1 - \frac{\pi}{2}\right), \quad (5)$$

where

$$\gamma_1 = \left[\frac{(1 - \cos\theta_1)^2(2 + \cos\theta_1)}{4}\right]^{1/3}. \quad (6)$$

Note that y_1^+ is negative for $\theta_1 < \frac{\pi}{2}$ (left picture on Fig. 2(b)) and positive otherwise. Note that $\alpha_1 = \pi/2$ for the first deposited droplet (see Fig. 2(b)).

3.2. Subsequent deposited droplets

For $j > 1$, and assuming that $R_{j-1} = R_j$ (hereafter, the parameters associated with the geometry of a deposited droplet $j > 1$ will be denoted, except for the contact angle between deposited droplets, by the subscript ∞), which, as will be discussed below, represents the main limitation of this model (see Fig. 3), Gao and Sonin [1] deduced the radius, R_∞, of the spheres fitted to the deposited droplets from the equivalent volume constraint of Eq. (2). This equation can be expressed as

$$\frac{4}{3}\pi R_{in}^3 = \frac{4}{3}\pi R_\infty^3 - \frac{\pi}{3}\left(R_\infty - \frac{1}{2}y_\infty\right)\left[3x_\infty^2 + \left(R_\infty - \frac{1}{2}y_\infty\right)^2\right], \quad (7)$$
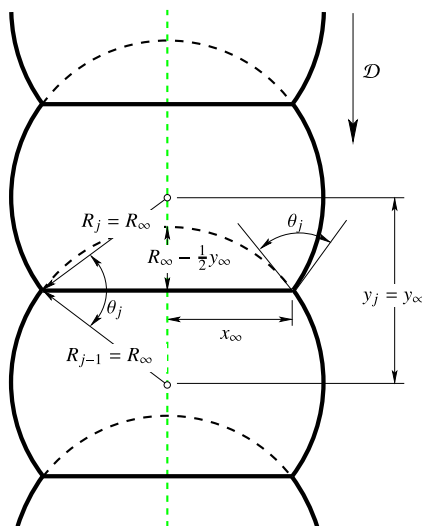

Fig. 3. Local geometry parameters for the subsequent deposited droplets proposed by Gao and Sonin [1].

where the last term is the volume of the intersection between the two spheres fitted to the deposited droplets $j - 1$ and j,

$$x_\infty = R_\infty \cos\frac{1}{2}\theta_j, \quad (8)$$

and

$$y_\infty = 2R_\infty \sin\frac{1}{2}\theta_j. \quad (9)$$

is the length added to the pillar, which would correspond to the distance between the centers of two consecutive deposited droplets. Introducing Eqs. (8) and (9) into Eq. (7) and arranging terms, yields

$$R_\infty = \frac{R_{in}}{\gamma_\infty} \quad (10)$$

and

$$y_\infty = 2\frac{R_{in}}{\gamma_\infty}\sin(\theta_j/2), \quad (11)$$

where

$$\gamma_\infty = \left[\frac{1}{2}\sin(\theta_j/2)\left(3 - \sin^2(\theta_j/2)\right)\right]^{1/3}. \quad (12)$$

Note that the above expressions only depend on R_{in} and θ_j and, as will be shown below, provide values that match with the asymptotic values obtained by using the proposed model, presented in Section 4, for sufficiently high j index values ($j \to \infty$).

The angle α_j can be obtained as

$$\alpha_j = \arccos\frac{\xi_j}{y_\infty}, \quad (13)$$

and the total length of the structure manufactured by deposition of n droplets can be obtained as

$$L_n = R_1 \sin\left(\theta_1 - \frac{\pi}{2}\right) + (n - 1)y_\infty + R_\infty, \quad (14)$$

where the first term on the right-hand side is the signed distance from the substrate to the center of the sphere fitted to the first deposited droplet (negative for $\theta_1 < \pi/2$ and positive otherwise).

3.3. Main limitations

Note that the assumption $R_j = R_{j-1}$ made by Gao and Sonin [1] only holds if the expressions of Eqs. (4) and (10) produce the same results, which would occur for cases in which the following volume-conservation parameter:

$$\mathscr{C} = \frac{1}{2}(1 - \cos\theta_1)^2(2 + \cos\theta_1) - \sin(\theta_j/2)\left(3 - \sin^2(\theta_j/2)\right) \quad (15)$$

equals zero. Fig. 4(a) represents the combination of angles θ_1 and θ_j for which $\mathscr{C} = 0$, and Fig. 4(b) shows the parameter $\mathscr{C}$ as a function of θ_1 and θ_j. As an example, Fig. 5 shows the volume error, E_V, as a function of θ_1 and θ_j for structures with $\xi_j = 0$ and $n = 2$ (slight variations of the results presented in Fig. 5 can appear with $n > 2$ and $\xi_j \neq 0$). This error is computed as the difference between the volume predicted by the model proposed in [1] and the volume of the deposited material. It can be seen that the volume errors can be very large for certain operating conditions.

Another important limitation of the Gao and Sonin [1] model is related to the imposed contact angle θ_j. For example, the angle θ_2^* (a similar analysis could have been made for $j > 2$) at the contact between the first spherical surface, of radius R_1 (Eq. (4)), and the second spherical surface, of radius R_∞ (Eq. (10)), whose centers are separated by a distance y_∞ (Eq. (11)), is (see Fig. 6(a))
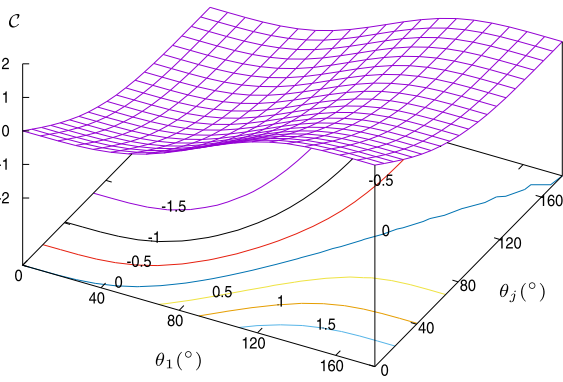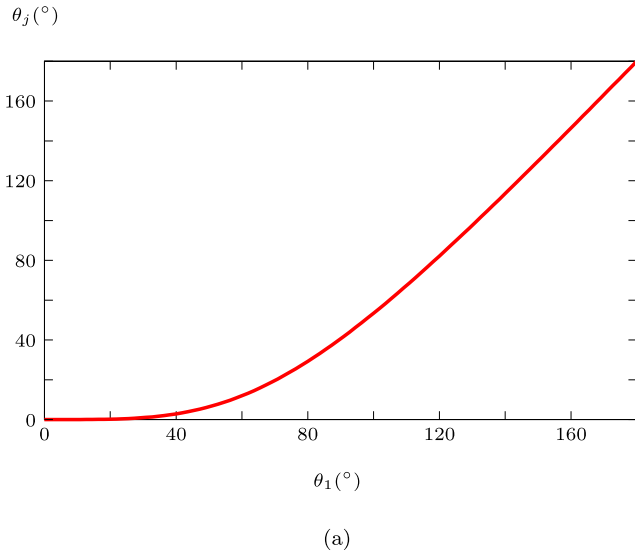
Fig. 4. Volume-conservation parameter $\mathscr{C}$. (a) Angle θ_j, as a function of θ_1, for which $\mathscr{C} = 0$. (b) $\mathscr{C}$ as a function of θ_1 and θ_j.
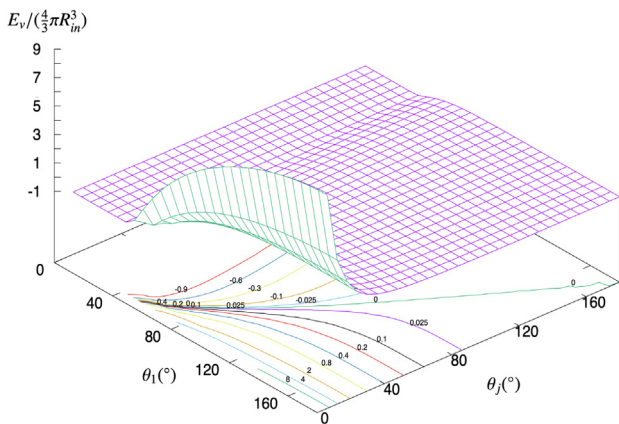

Fig. 5. Volume error, E_v, as a function of θ_1 and θ_j for structure geometries predicted by the model proposed in [1] with $\xi_j = 0$ and $n = 2$.

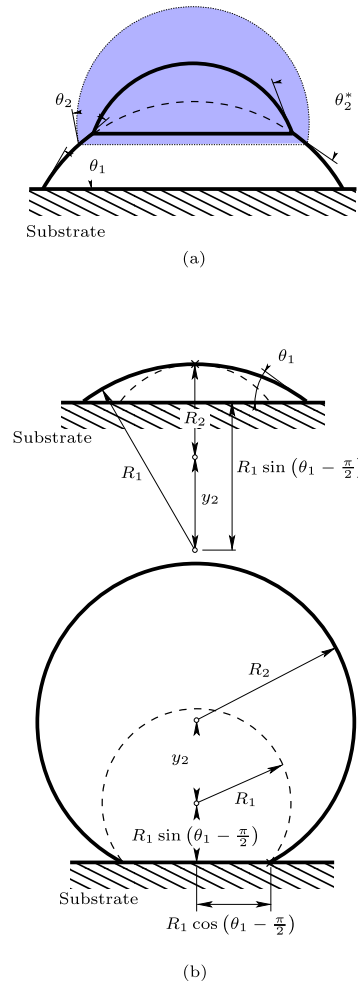$$\theta_2^* = \arccos\left(\frac{R_\infty^2 + R_1^2 - y_\infty^2}{2R_\infty R_1}\right). \tag{16}$$

Fig. 6. Examples of limitations of the model proposed in [1] for $\xi_2 = 0$. (a) The resulting angle θ_2^* does not match the angle θ_2 introduced in the model and the volume of the second droplet is not correct (the correct volume is highlighted by the blue shaded region). (b) Limiting cases for which the model predicts no contact between the first two deposited droplets (cases for $\theta_1 < \pi/2$ on the top and $\theta_1 > \pi/2$ on the bottom).

Note that θ_2^* does not necessarily coincide with the imposed value of the contact angle θ_2 introduced in Eqs. (10) and (11). Moreover, for certain conditions the results provided by these equations even produce no contact between deposited droplets (see the examples in Fig. 6(b)), situations that occur when

$$\left[R_1 \cos\left(\theta_1 - \frac{\pi}{2}\right)\right]^2 + \left[R_1 \sin\left(\theta_1 - \frac{\pi}{2}\right) + y_\infty\right]^2 - R_\infty^2$$
$$< 0, \text{ for } \theta_1 > \pi/2. \tag{17}$$

(bottom picture in Fig. 6(b)), or

$$(R_1 - y_\infty)^2 - R_\infty^2 > 0, \text{ for } \theta_1 < \pi/2 \tag{18}$$

(top picture in Fig. 6(b)). Fig. 7 shows the angle error $E_\theta = \theta_2 - \theta_2^*$ as a function of θ_2, for different θ_1 values. Note that E_θ, which increases as θ_2 increases and θ_1 decreases, can be considerably high, leading to a very inaccurate prediction of the geometry of the manufactured structure.

In this work, a new analytic model that strictly conserves the volume and exactly matches the contact angle between consecutive droplets is presented in the next section. To our best knowledge, this is the first strictly conservative analytic model able to
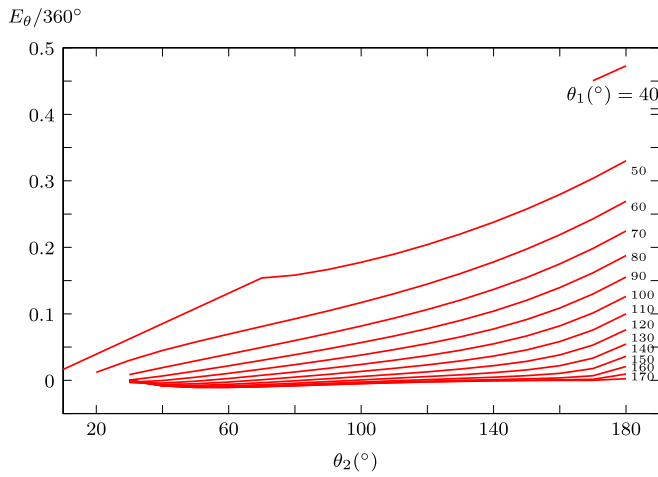
Fig. 7. Error E_θ, obtained using the model proposed in [1], as a function of θ_2, for different values of θ_1.

accurately determine the geometry of structures manufactured under dropwise deposition conditions.

4. Proposed model

A molten droplet j (from 2 to n) of initial radius R_{in} is deposited along the direction $\mathscr{D}$ over a previously solidified droplet, fitted to a sphere of radius R_{j-1}, with a deposition spacing ξ_j (see Fig. 8(a)). The centers O_{j-1} and O_j of the spheres fitted to the deposited droplets $j-1$ and j, respectively, and the contact line C_j between both droplets are marked in Fig. 8(b) with open circles. It can easily be deduced that the segments $\overline{O_{j-1}C_j}$ and $\overline{O_jC_j}$, with lengths R_{j-1} and R_j, respectively, define an angle equal to the contact angle θ_j formed by the deposited droplets j and $j-1$. The closest distance, x_j, from the contact line C_j to $\overline{O_{j-1}O_j}$ can be obtained as

$$x_j = R_j \cos \theta_j^+, \tag{19}$$

or

$$x_j = R_{j-1} \cos \theta_j^-, \tag{20}$$

where θ_j^- and θ_j^+ are, respectively, the angles defined by $\overline{O_{j-1}C_j}$ and $\overline{O_jC_j}$ with the line perpendicular to $\overline{O_{j-1}O_j}$. Taking into account that

$$\theta_j^+ + \theta_j^- = \theta_j, \tag{21}$$

introducing $\theta_j^- = \theta_j - \theta_j^+$ into Eq. (20) and equating Eqs. (19) and (20), it can be obtained that

$$R_j \cos \theta_j^+ = R_{j-1} \cos \theta_j \cos \theta_j^+ + R_{j-1} \sin \theta_j \sin \theta_j^+, \tag{22}$$

and, arranging terms, it can be written that

$$\tan \theta_j^+ = \frac{R_j - R_{j-1} \cos \theta_j}{R_{j-1} \sin \theta_j}. \tag{23}$$

Similarly, introducing $\theta_j^+ = \theta_j - \theta_j^-$ into Eq. (19) and equating Eqs. (19) and (20), it can be obtained that

$$\tan \theta_j^- = \frac{R_{j-1} - R_j \cos \theta_j}{R_j \sin \theta_j}. \tag{24}$$

Thus, the length $y_j = y_j^+ + y_j^-$, corresponding to the distance between the centers of the spheres fitted to the two deposited droplets, can be expressed as

$$y_j = \underbrace{x_j \tan \theta_j^+}_{y_j^+} + \underbrace{x_j \tan \theta_j^-}_{y_j^-}. \tag{25}$$

The length y_j can also be expressed as

$$y_j = \left(R_j^2 + R_{j-1}^2 - 2R_jR_{j-1} \cos \theta_j \right)^{1/2}, \tag{26}$$

and equating Eqs. (26) and (25), the following expression for x_j can be obtained:

$$x_j = \frac{\left(R_j^2 + R_{j-1}^2 - 2R_jR_{j-1} \cos \theta_j \right)^{1/2}}{\tan \theta_j^+ + \tan \theta_j^-}. \tag{27}$$
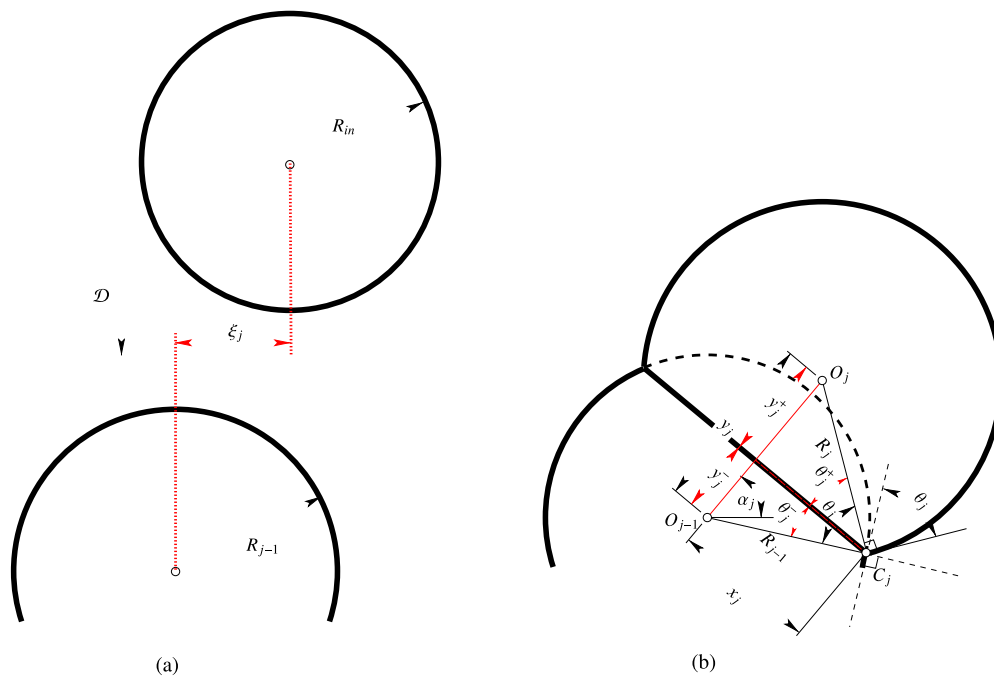

Fig. 8. Subsequent deposited droplet ($j > 1$). (a) Before and (b) after the deposition.

Thus,

$$y_j^+ = \left(R_j^2 + R_{j-1}^2 - 2R_jR_{j-1}\cos\theta_j\right)^{1/2} \frac{\tan\theta_j^+}{\tan\theta_j^+ + \tan\theta_j^-}, \tag{28}$$

and

$$y_j^- = \left(R_j^2 + R_{j-1}^2 - 2R_jR_{j-1}\cos\theta_j\right)^{1/2} \frac{\tan\theta_j^-}{\tan\theta_j^+ + \tan\theta_j^-}. \tag{29}$$

Introducing Eqs. (23) and (24) into Eqs. (27)–(29), the parameters x_j, y_j^+ and y_j^- can be obtained as a function of R_{j-1}, R_j and θ_j, respectively, as

$$x_j = \frac{R_jR_{j-1}\sin\theta_j}{\left(R_j^2 + R_{j-1}^2 - 2R_jR_{j-1}\cos\theta_j\right)^{1/2}}, \tag{30}$$

$$y_j^+ = \frac{R_j^2 - R_jR_{j-1}\cos\theta_j}{\left(R_j^2 + R_{j-1}^2 - 2R_jR_{j-1}\cos\theta_j\right)^{1/2}}, \tag{31}$$

and

$$y_j^- = \frac{R_{j-1}^2 - R_jR_{j-1}\cos\theta_j}{\left(R_j^2 + R_{j-1}^2 - 2R_jR_{j-1}\cos\theta_j\right)^{1/2}}. \tag{32}$$

Finally, by equating the liquid volume of the incoming droplet with the volume of the deposited droplet j, the following expression can be written (see the volume decomposition shown in Fig. 9):

$$\frac{4}{3}\pi R_{in}^3 = \frac{4}{3}\pi R_j^3 - \underbrace{\frac{\pi}{6}\left(R_{j-1} - y_j^-\right)\left[3x_j^2 + \left(R_{j-1} - y_j^-\right)^2\right]}_{\text{top spherical cap volume}}$$
$$- \underbrace{\frac{\pi}{6}\left(R_j - y_j^+\right)\left[3x_j^2 + \left(R_j - y_j^+\right)^2\right]}_{\text{bottom spherical cap volume}}. \tag{33}$$

From Fig. 8(b), it is easy to be deduced that the heights of the top and bottom spherical caps depicted in Fig. 9 are, respectively, $R_{j-1} - y_j^-$ and $R_j - y_j^+$. Introducing Eqs. (30)–(32) into Eq. (33), the solution for R_j is found using a Newton–Raphson iteration procedure until a precise tolerance of 10^{-10} is reached.
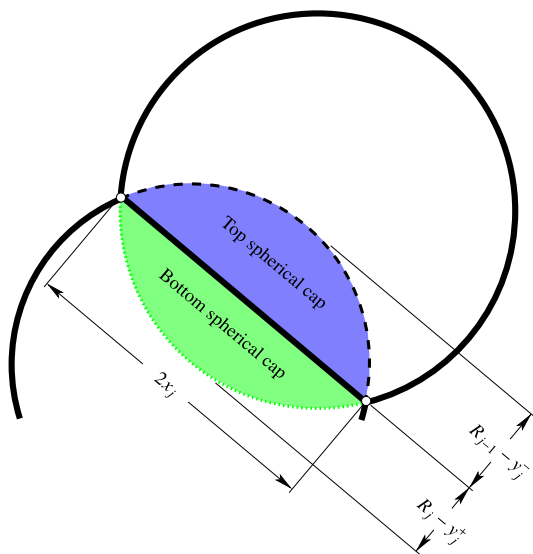

Fig. 9. Volume decomposition in the expression of Eq. (33).

Also, y_j can be obtained by introducing the solution for R_j into Eq. (26), and finally α_j can also be obtained as

$$\alpha_j = \arccos\frac{\xi_j}{y_j}. \tag{34}$$

The total length L_n can be obtained as

$$L_n = R_1 \sin\left(\theta_1 - \frac{\pi}{2}\right) + \sum_{j=2}^{n} y_j + R_n, \tag{35}$$

where the first term is the signed distance from the substrate to the center of the sphere fitted to the first deposited droplet, the second term is the sum of lengths of the segments that join the centers of the spheres fitted to consecutive deposited droplets from $j = 2$ to n, and the last term is the radius of the sphere fitted to the last deposited droplet n.

4.1. Limiting condition for drop-on-drop deposition

If the droplet deposition spacing ξ_j reaches a certain limiting value, the deposited droplet j may encounter the deposited droplet $j - 2$ (substrate for $j = 2$). Fig. 10 shows two examples of this lim-
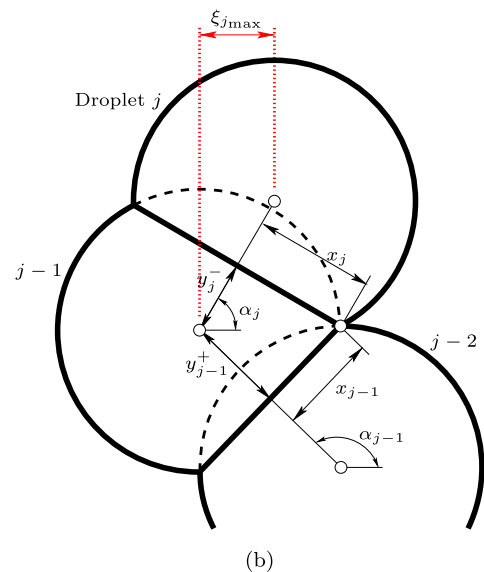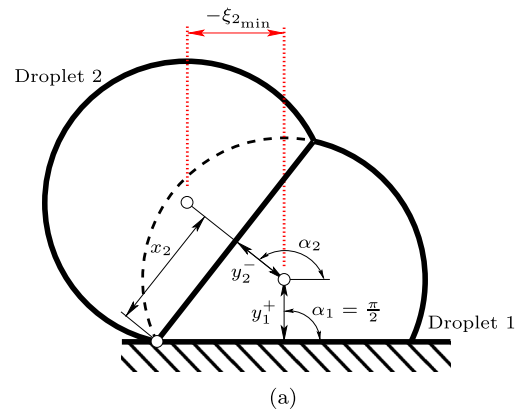

(a)

(b)

Fig. 10. Examples of limiting conditions for drop-on-drop deposition. Triple contact between (a) droplets $2, 1$ and the substrate, and between (b) droplets $j, j - 1$ and $j - 2$.

iting condition. In the example for $j = 2$ (Fig. 10(a)), this situation occurs if

$$y_1^+ + y_2^- \sin \alpha_2 = -x_2 \cos \alpha_2, \tag{36}$$

and in the example for $j > 2$ (Fig. 10(b)), if

$$y_{j-1}^+ \sin \alpha_{j-1} + y_1^- \sin \alpha_j = -x_{j-1} \cos \alpha_{j-1} + x_j \cos \alpha_j. \tag{37}$$

Introducing Eq. (34) into Eqs. (36) and (37) and solving for the droplet deposition spacing, one can obtain the limits $\xi_{2_{\min}}$ and $\xi_{j_{\max}}$ that must be used to avoid the deposited droplet j from contacting the substrate or the droplet $j - 2$, respectively.

5. Thermal model

The one-dimensional heat transfer model proposed in [22] is considered to obtain the temperature evolution at the tip of a column during its construction. The results of this model will be used to verify that the thermal assumptions considered in this work are satisfied during the experiments carried out to build columns under different operating conditions. A brief description of this model is shown below.

The temperature at the tip just before a new incoming droplet j is deposited on it (see Fig. 11) is computed as follows. The column obtained by drop-on-drop deposition of the previously deposited $j - 1$ droplets is assumed to be a cylinder of L_{j-1} length and $\overline{R}_{j-1}$ radius calculated as follows. Based on the temperature measurements made in [22], convective heat loss from the column to the surrounding air was found to be negligible and the heat flux q transferred by conduction from the tip of column to the substrate can be obtained as

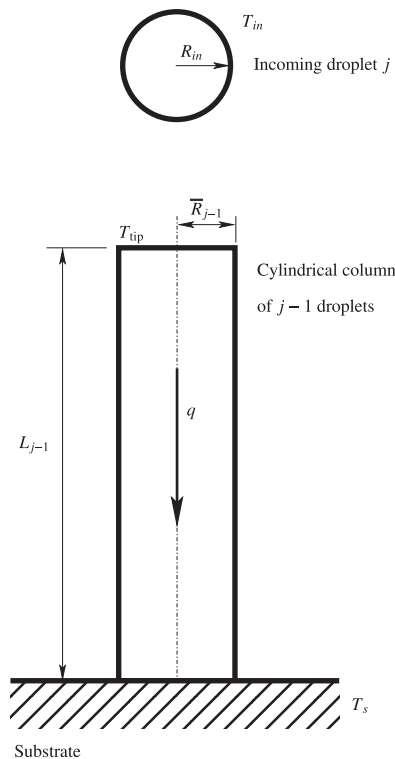$$q = \frac{T_{\text{tip}} - T_s}{R_s + L_{j-1}/k} \pi \overline{R}_{j-1}^2, \tag{38}$$

where T_{tip} is the temperature at the tip of the column, T_s is the substrate temperature, R_s is the thermal contact resistance at the interface between the substrate and the column, and L_{j-1}/k is the thermal resistance of the pre-deposited column of $j - 1$ droplets.

The length of the cylindrical column is obtained as

$$L_{j-1} = R_1 \sin \left(\theta_1 - \frac{\pi}{2} \right) + \sum_{j'=2}^{j-1} y_{j'} + R_{j-1}. \tag{39}$$

Note that the volume V_{j-1} of the column constructed from $j - 1$ droplets must be equal to

$$V_{j-1} = (j-1) \frac{4}{3} \pi R_{in}^3. \tag{40}$$

Equating this volume to the volume $L_{j-1} \pi \overline{R}_{j-1}^2$ of the cylindrical column used in the thermal model, the average radius $\overline{R}_{j-1}$ can be obtained as

$$\overline{R}_{j-1} = \left[(j-1) \frac{4}{3} \frac{R_{in}^3}{L_{j-1}} \right]^{1/2}. \tag{41}$$

The thermal energy rate due to the incoming droplet can be obtained as

$$E = f \frac{4 \rho \pi R_{in}^3}{3} \left[c \left(T_{in} - T_{\text{tip}} \right) + H \right], \tag{42}$$

where T_{in} is the temperature of the incoming droplet j, f is the deposition frequency and ρ, c and H are, respectively, density, specific heat, and latent heat of fusion of the deposited material.

Equating Eqs. (38) and (42), the temperature of the column tip can be obtained as

$$T_{\text{tip}} = \frac{c T_{in} + \beta T_s + H}{c + \beta}, \tag{43}$$

where

$$\beta = \frac{\overline{R}_{j-1}^2}{f \frac{4}{3} \rho R_{in}^3 \left(R_s + L_{j-1}/k \right)}.$$

6. Experiments

To validate the proposed model, several experiments were carried out for the manufacturing of vertical columns using two different deposition materials:

1. a paraffin and
2. a low melting point metal alloy,

which produce contact angles, θ_1, lower and higher than about 90°, respectively. In this way, the differences in trends dependent on the value of θ_1 observed in the results presented in Section 7 can be analyzed.

Two different materials are considered for the substrate:

1. a stainless-steel plate (polished AISI 316L) for both droplet materials and
2. a PVC plate for the paraffin droplets.

The arithmetic mean deviation, R_a, of the surface profile evaluated on both plates was measured with the SM Metrology Pl100/BR rugosimeter, obtaining values of 0.253 μm and 1.548 μm for the stainless-steel and PVC plates, respectively. All the experiments were made with a substrate temperature equal to 296 K.

Fig. 11. Thermal model.

Table 1
Physical properties of paraffin and Field's alloy.

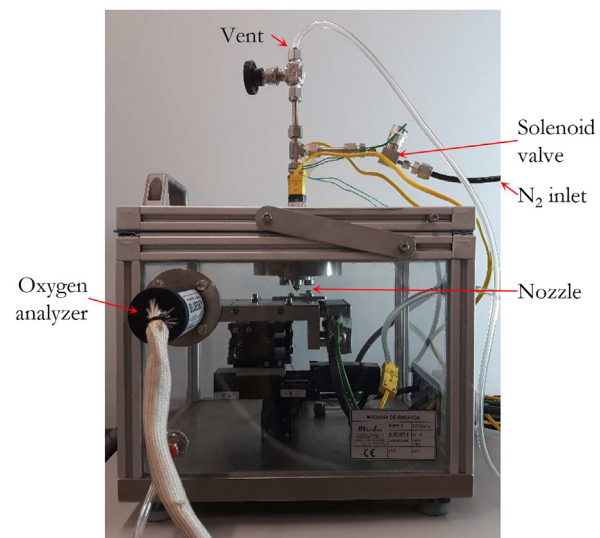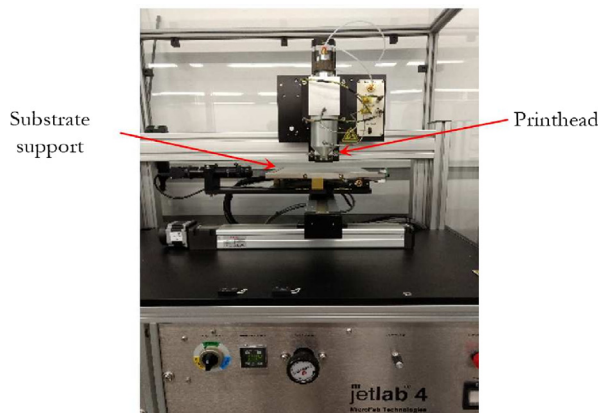| Droplet material	Melting temperature (K)	Density (kg m^{-3})	Specific heat (J kg^{-1} K^{-1})	Thermal conductivity (W m^{-1} K^{-1})	Latent heat of fusion (J kg^{-1})	Dynamic viscosity (Pa s)	Surface tension (N m^{-1})
Paraffin	342.4	771.0	2560.0	0.237	226.0×10^3	5.4×10^{-3}	22.4×10^{-3}
Field's alloy	333.0	7880.0	170.5	34.5	40.2×10^3	2.0×10^{-3}	4.3×10^{-1}

Fig. 12. Drop-on-demand print station used for paraffin (top photo) and metal (bottom photo) droplet generation.

6.1. Experiments with paraffin

A fully refined paraffin wax (1260A, manufactured by the International Group, Inc.) is used. Table 1 shows the physical properties of the paraffin [31]. The droplets were generated in a drop-on-demand print station (JetLab4 XL, manufactured by MicroFab Technologies, Inc.) which is equipped with a high temperature printhead (PH-04a polymer jet) and a piezoelectric dispensing device (MJ-SF-04–50-6MX) with an orifice diameter of 50 μm (left photo in Fig. 12). The temperature of the printhead was set to 358 K, and a dwell and an echo voltage of 100 V and 70 V, respectively, were set in the printhead control. The distance from the nozzle to the substrate was set to 3 mm. The droplets were generated with a frequency of 1 Hz and acquired a velocity of around $U_{in} = 1.75$ m s^{-1} just before impact.

6.2. Experiments with a low melting point metal alloy

Field's metal alloy (51% indium, 32.5% bismuth, and 16.5% tin) is used. Table 1 shows the physical properties of the alloy (see, for
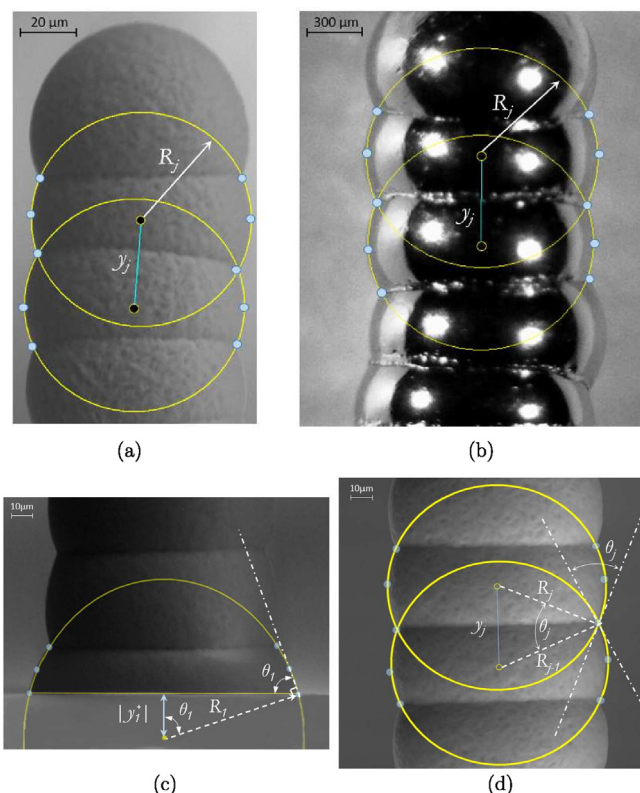

Fig. 13. Schematic examples of the procedures used for the indirect R_{in} estimation of (a) paraffin and (b) Field's alloy droplets, and for the measurement of solidification contact angles (c) θ_1 and (d) θ_j.

example, [33]). An improved version of the drop-on-demand print station developed in [32], which incorporates a faster solenoid valve and new nozzles, was used for the generation and deposition of small droplets (right photo in Fig. 12). Each droplet is released by applying a of 6 ms and 0.1 MPa pressure pulse with nitrogen gas that pushes the molten metal contained in the furnace and forces the generation of the droplet through a nozzle. In all experiments, the molten metal temperature in the furnace was set to 353 K. The distance from the nozzle to the substrate was 8.5 mm. Droplets were generated with a frequency of 0.1 Hz, using a 0.67 mm diameter nozzle, and acquired a velocity of around $U_{in} = 0.29$ m s^{-1} just before impact. To minimize oxidation effects on the metal droplets, the O$_2$ content in the chamber where the droplets were generated was kept below 170 ppm.

6.3. Measurement procedure

All recorded images of the manufactured vertical columns were post-processed using the public-domain software ImageJ [34] to measure their geometry. The images of the paraffin droplets were acquired using a scanning electron microscope (Hitachi S-3500 N) with backscattered electrons, a low vacuum pressure of 70 Pa and an accelerating voltage of 15.0 kV. A magnification of 700 was used, resulting in an image resolution of 0.0713 μm/pixel. In the

Table 2

Estimated values of R_{in}, and the corresponding 95% confidence intervals in the experiments performed with paraffin and Field's alloy.

Droplet material	R_{in} (μm)
Paraffin	40.0 ± 0.1
Field's alloy	764.5 ± 12.5

Table 3

Values of the contact angle θ_1 (the corresponding 95% confidence intervals are also indicated) for paraffin and Field's alloy droplets.

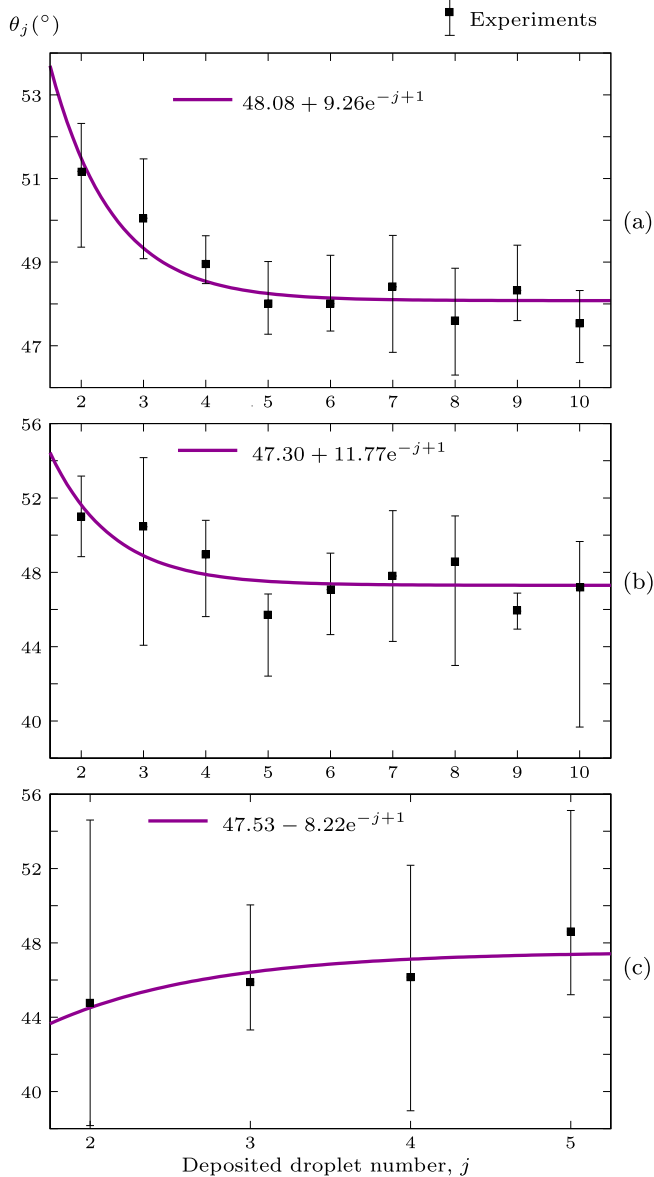|	θ_1 (°)
Paraffin droplets on AISI plates	73.9 ± 1.8
Paraffin droplets on PVC plates	65.1 ± 2.0
Field's alloy droplets on AISI plates	100.5 ± 2.5

Fig. 14. Average values of the measured contact angle θ_j, along with the corresponding fitting curves. (a) Paraffin columns over AISI plates. (b) Paraffin columns over PVC plates. (c) Field's alloy columns over AISI plates.
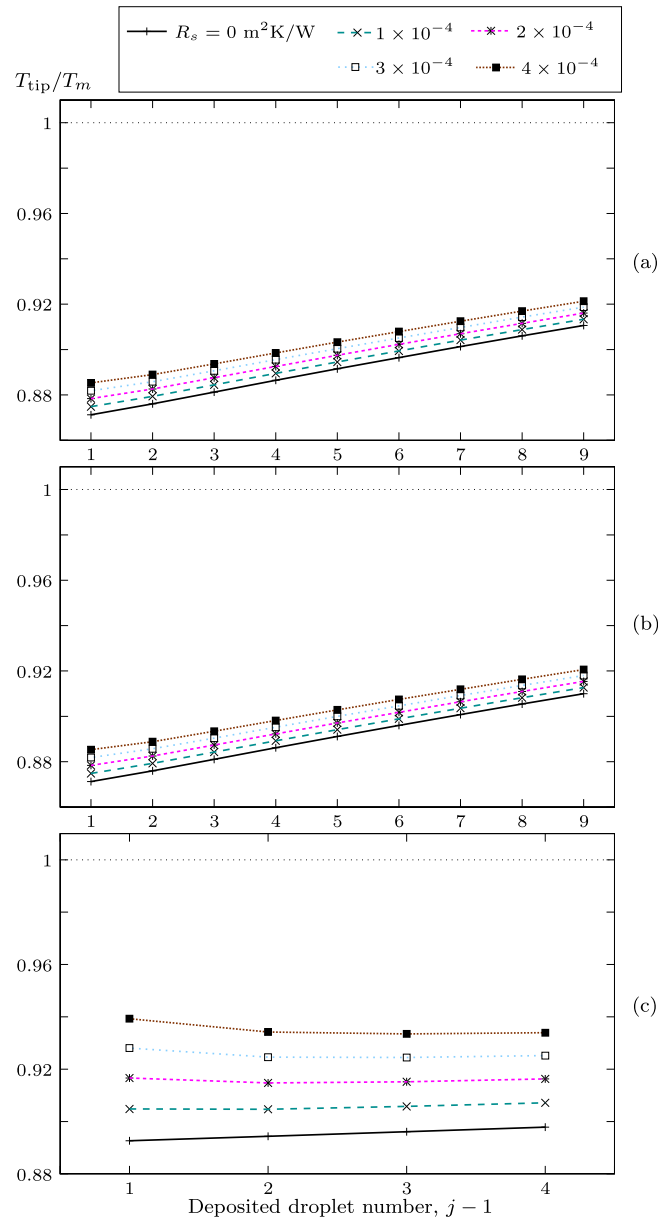
Table 4

Ranges of the main time scales (ms) for the operating conditions considered in the experiments.

Impact, $\tau_k \sim 2R_{in}/U_{in}$	Inertial-capillarity, $\tau_\sigma \sim \left(\rho R_{in}^3/\sigma\right)^{1/2}$	Solidification, $\tau_{\mathrm{sol}} \sim \frac{R_{in}^2 H}{\alpha c (T_m - T_0)}$
$0.05 \div 3$	$0.05 \div 3$	$26 \div 163$

Fig. 15. Evolution of the dimensionless column tip temperature. (a) Paraffin column on AISI substrate. (b) Paraffin column on PVC substrate. (c) Field's alloy column on AISI substrate.

case of Field's alloy droplets, the images were acquired using a conventional microscope (Olympus BX53M), which produces an image resolution of 7.2 μm/pixel.

The following four parameters are used to describe the column shape:

1. radius, R_{in}, of the incoming droplet,
2. radius, R_j, of the sphere fitted to the deposited droplet j on the manufactured column,

3. contact angle θ_1, and
4. contact angle θ_j.

The parameters are determined from the circles that best fit the recorded images using the procedure described below.

6.3.1. Best fit circle

A best fit circle, given by the coordinates of its center and radius, is obtained from the recorded image of a deposited droplet using six equidistant points located along its visible interface surface. The geometric parameters listed above are obtained from the values averaged over four to five different columns manufactured under the same operating conditions. Fig. 13 shows some examples of the fitting procedure performed over several recorded images.

Droplet radius measurement The small size and high velocity of the incoming droplet make it difficult to use direct visualization methods to accurately estimate its radius, R_{in}. Instead, assuming that (1) the deposited droplets reach a quasi-spherical shape, (2) the volume contraction during the cooling and solidification of the droplet is negligible, and (3) any gaps, such as porosity or gas trapped bubbles, within the deposited droplet can be considered negligible, the following indirect procedure is used. The radius of the incoming droplet, R_{in}, is estimated from the measurement of

the radius R_j and the distance y_j, where j is high enough to reach the corresponding asymptotic constant value ($R_j \simeq R_\infty$), as

$$R_{in} = \frac{1}{2}\left(6R_j^2 y_j - \frac{1}{2}y_j^3\right)^{1/3}. \tag{44}$$

A schematic of this indirect measurement procedure for paraffin and Field's alloy is shown in Figs. 13(a) and 13(b), respectively. Measurements on several columns manufactured under the same operating conditions provide the results presented in Table 2.

Measurement of contact angles The contact angle, θ_1, is estimated as (see the example in Fig. 13(c))

$$\theta_1 = \arccos\left(-\frac{y_1^+}{R_1}\right), \tag{45}$$

where R_1 is the radius of the circle best fitted to the recorded image of the first deposited droplet and y_1^+ is the signed distance from the best fit circle center to the substrate line. This substrate line is traced by joining the two points of the contact line where the deposited droplet, air and substrate meet in the plane of the recorded image. Note that y_1^+ is considered negative if the center of the best circle fitted to the first droplet is below the substrate line and positive otherwise. Table 3 shows the θ_1 values estimated for the experiments made with paraffin droplets over AISI and PVC
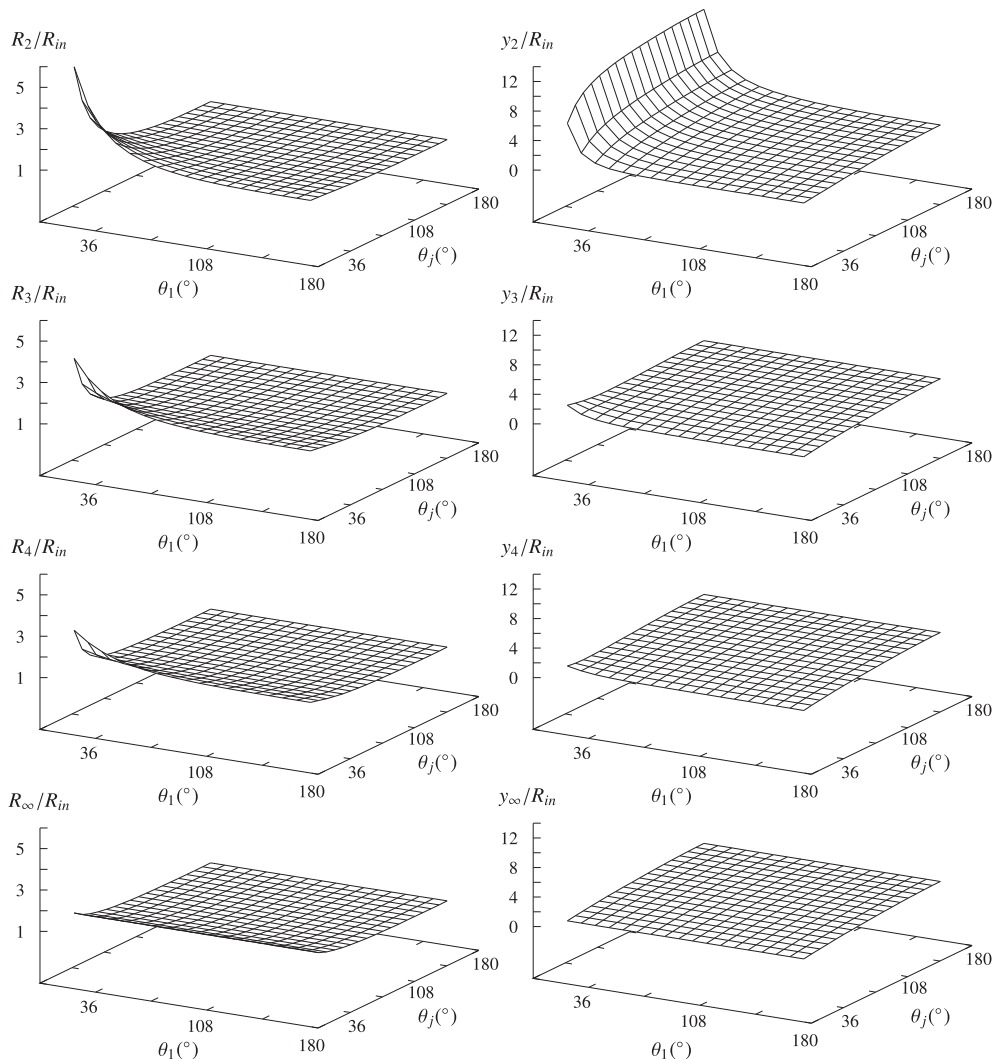

Fig. 16. R_j/R_{in} (left column) and y_j/R_{in} (right column) as a function of θ_1 and θ_j, for $j = 2, 3, 4$. The bottom picture in both columns corresponds to the asymptotic ($j \to \infty$) results [1].
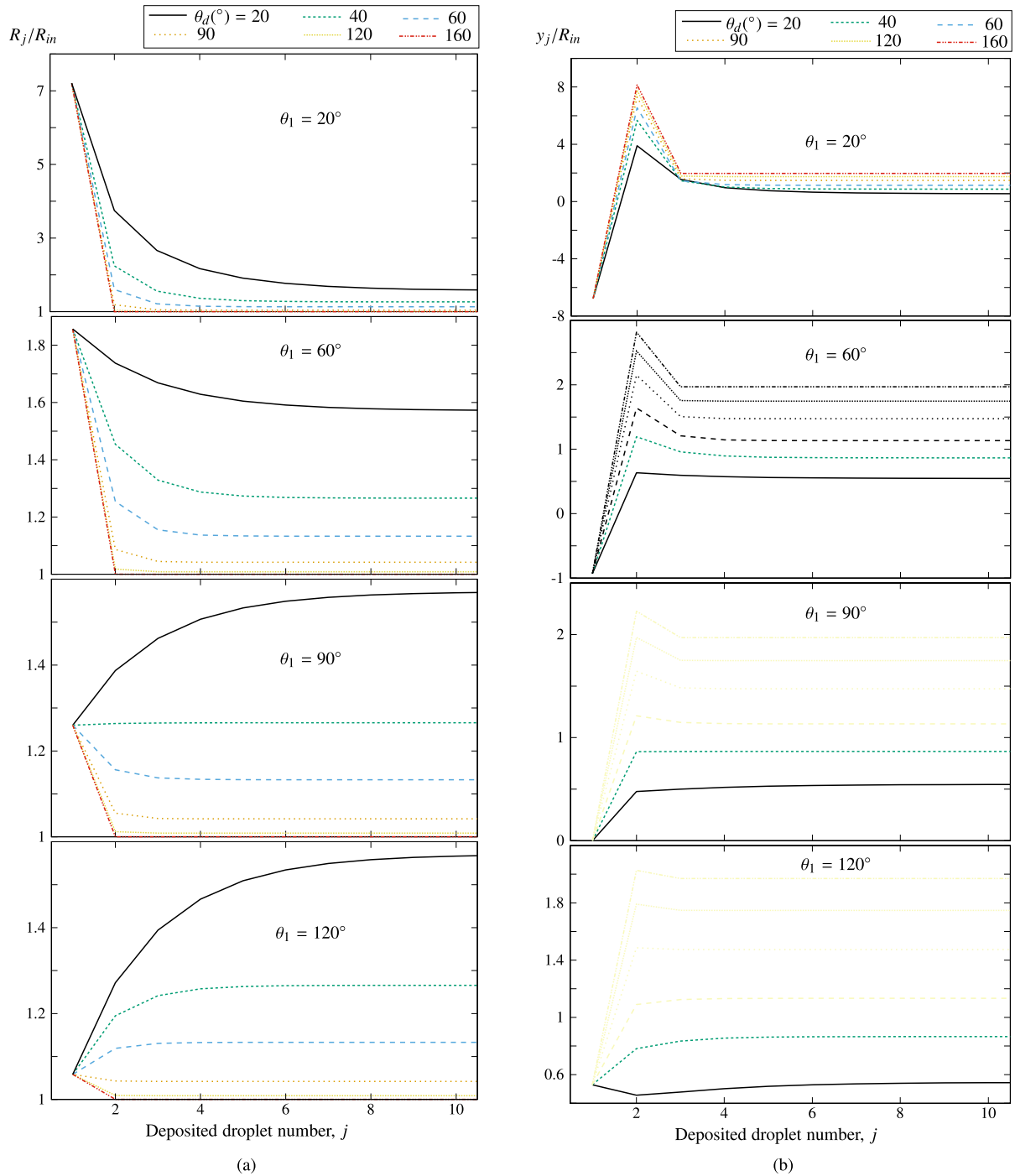
Fig. 17. R_j/R_{in} (a) and y_j/R_{in} (b) as a function of j for different values of θ_1 and a constant $\theta_j = \theta_d$ for $j > 1$.

plates and with Field's alloy droplets over AISI plates. Using a similar procedure, the contact angle θ_j is estimated from measurements made over the recorded images as (see the example in Fig. 13(d))

$$\theta_j = \arccos \frac{R_{j-1}^2 + R_j^2 - y_j^2}{2R_{j-1}R_j}. \tag{46}$$

Fig. 14 shows the average values of the measured angle θ_j as a function of j. The averaging was performed on a series of about five columns built repeatedly under the same conditions. The maximum and minimum measured values are also represented by vertical error intervals. Exponential functions of the type

$$\theta_j = A + Be^{-j+1} \tag{47}$$

have been fitted to the average θ_j values, and the corresponding expressions are represented in the figure with continuous lines. It can be observed that, starting from the third (Fig. 14(c)) or fourth (Figs. 14(a) and 14(b)) droplet on the column, θ_j reaches an almost constant average value. This behavior may be due to the fact that a steady-state thermal condition could have been reached approximately at the tip of the columns during dropwise deposition for sufficiently high j values.

6.4. Operating conditions analysis

Under the operating conditions considered in this work, the Bond number, $Bo = \rho g R_{in}^2/\sigma$, where g is the acceleration of gravity

and σ is the surface tension coefficient between the molten droplet material and the ambient aire, varies from 5.5×10^{-4} to 10^{-1}, a range for which the gravitational effects are negligible, and the Weber number, $We = \rho U_{in}^2 R_{in}/\sigma$, varies from 1.2 to 4.3, a range for which quasi-spherical shapes of the deposited molten droplets are reached while maintaining good ballistic accuracies during droplet impacts. Table 4 shows a rough estimate of the ranges of time scales involved in the experiments. Note that the solidification time scale ($\tau_{sol} \sim \frac{R_{in}^2 H}{\alpha c(T_m - T_0)}$, where T_m is the melting temperature of the droplet material) is substantially larger (almost two orders of magnitude) than those involved in the droplet impact dynamics ($\tau_k + \tau_\sigma$), thus quasi-spherical shapes of the solidified droplets are also expected to appear in the experiments.

Estimates of the column tip temperature using the one-dimensional analytical heat transfer model of Section 5 indicate that deposition frequencies of 1 and 0.1 Hz for paraffin and Field's

alloy droplets, respectively, are low enough to ensure that incoming droplets always impact on the column tip on a completely solidified pre-deposited droplet. Fig. 15 shows the evolution, as drops are deposited, of the dimensionless column tip temperature for different values of the contact thermal resistance, R_s. It should be mentioned that an accurate estimation of the contact thermal resistance involved in the experiments is not a simple task, although approximate R_s values can be found in the literature for relatively similar operating conditions. For example, based on the experimental measurements of [31], the thermal contact resistance between wax droplets and an aluminum substrate can be considered negligible ($R_s \simeq 0$), and based on the experimental observations of [35], the authors of [22] considered an approximated value of $R_s \simeq 10^{-4}$ m²K/W for tin droplets impinging on a nickel substrate. In any case, it can be seen from the results presented in Fig. 15 that for the experimental conditions considered in this work and sufficiently wide ranges of R_s values (from 0 to
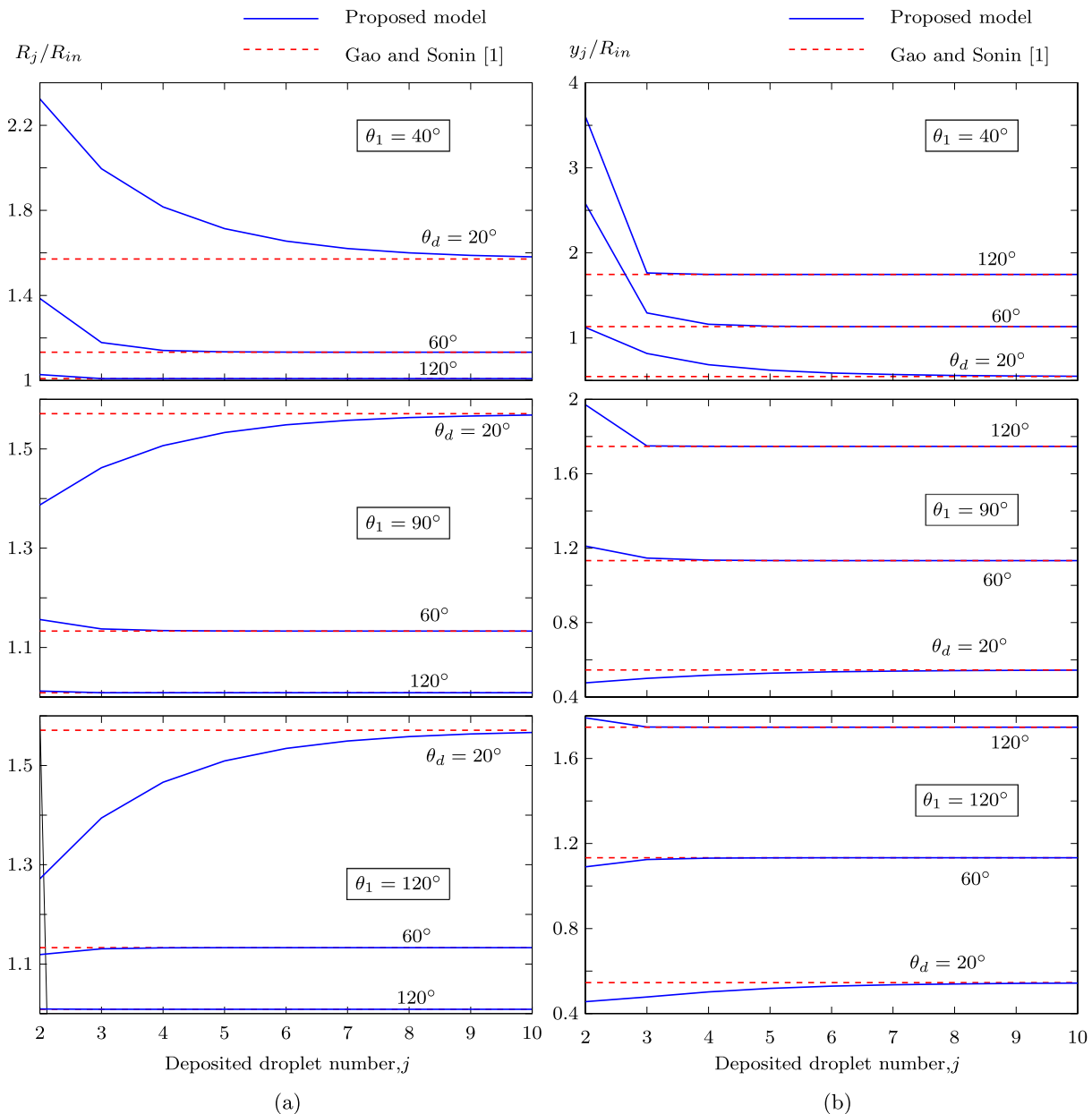

Fig. 18. R_j/R_{in} (a) and y_j/R_{in} (b) as a function of j for different values of θ_1 and a constant $\theta_j = \theta_d$ for $j > 1$. Comparison between the results predicted by the proposed model and the model proposed in [1].

4×10^{-4} m^{2}K/W), the temperature at the tip of the column always remains below T_m just before a new droplet j is deposited on it. The deposition frequency above which the complete solidification of pre-deposited droplets cannot be ensured is about 4 Hz for paraffin columns with $R_s = 0$ and about 0.5 Hz for Field's alloy columns with $R_s = 2 \times 10^{-4}$ m^{2}K/W.

7. Results and discussion

In the following sections, an assessment of the proposed geometrical model will be presented, comparing its results with the corresponding asymptotic values (Section 7.1), which coincide with those of the Gao and Sonin [1] model, and with experimental

results (Section 7.2) for wide ranges of operating conditions. Also, an example of industrial interest is presented in Section 7.3.

7.1. Comparison with asymptotic results

Fig. 16 shows the dimensionless radius of the sphere fitted to the deposited droplet j (left column) and distance between the centers of the spheres fitted to the deposited droplets j and $j - 1$ (right column) as a function of the contact angles θ_1 and θ_j, for $j = 2, 3, 4$. The bottom image in both columns corresponds to results obtained for a sufficiently high deposited droplet index j ($j \to \infty$), for which the asymptotic values matching those of the model proposed in [1] are reached (it can be observed that these results do not depend on
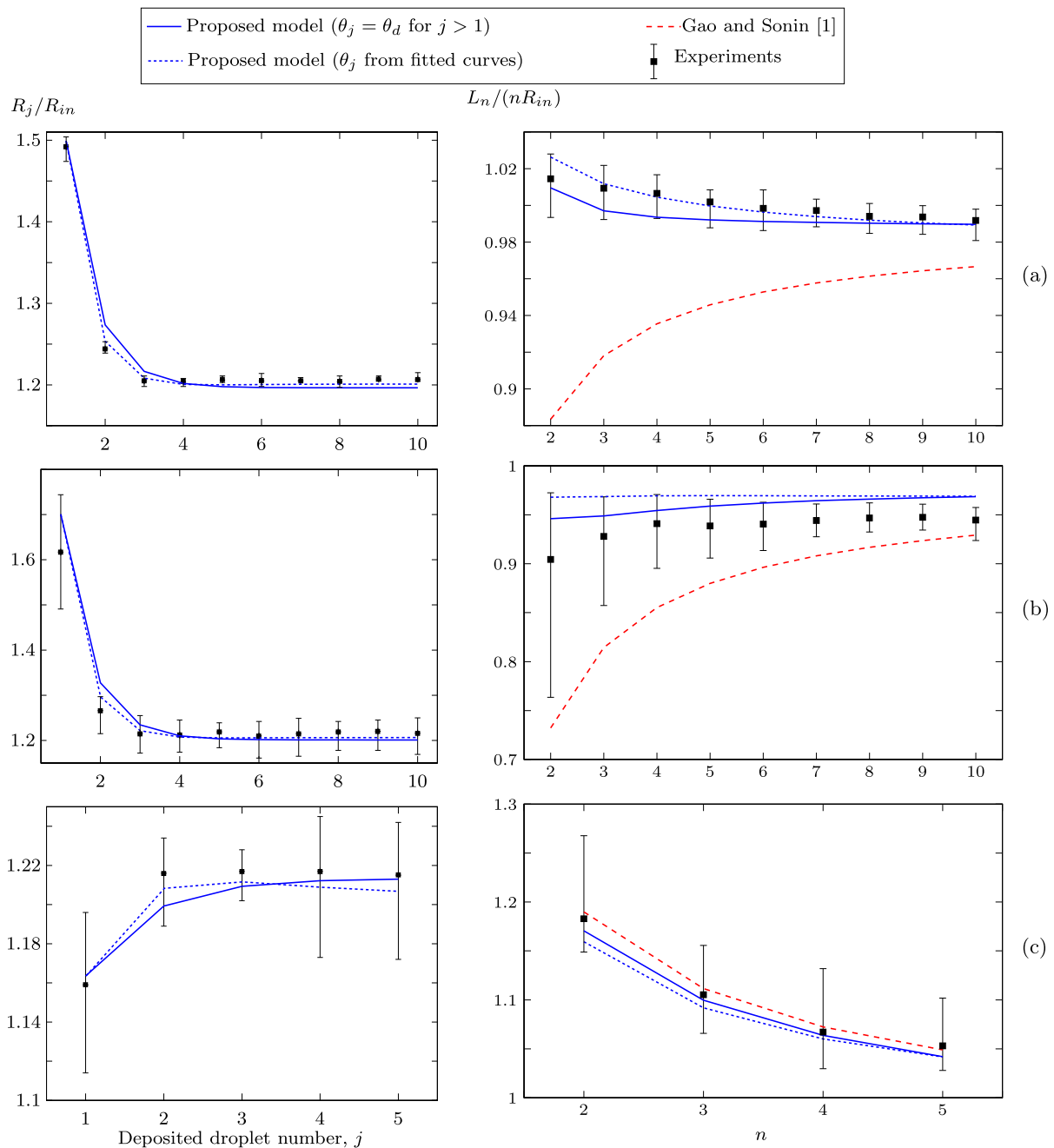

Fig. 19. Comparison between experimental and theoretical results for R_j/R_{in} as a function of j (pictures on the left) and for $L_n/(nR_{in})$ as a function of n (pictures on the right) for columns manufactured with different materials. (a) Paraffin columns on an AISI plate. (b) Paraffin columns on a PVC plate. (c) Field's alloy columns on an AISI plate. The constant $\theta_j = \theta_d$ is the average of the measured values in the column for $j > 1$.

θ_1). The results obtained with the proposed model reveal visually significant differences with the asymptotic results, which are more evident as the contact angles and index j decrease. It can also be observed that the convergence to the asymptotic value as the index j increases is faster for the distance y_j than for the radius R_j.

To better observe the variations of R_j and y_j along the length of the manufactured columns, Figs. 17(a) and 17(b) show R_j/R_{in} and y_j/R_{in}, respectively, as a function of j for different values of θ_1 and θ_j. It can be seen from Fig. 17(a) that the asymptotic R_∞ value is reached from a value of j which increases as θ_j decreases (about 8 for $\theta_j = 20°$). Significant variations for y_j along the column height can also be observed in Fig. 17(b), although the asymptotic value y_∞ is reached for lower values of j.

Figs. 18(a) and 18(b) directly compare the asymptotic values predicted by the model proposed in [1] (dashed horizontal lines) with those of the proposed model represented in Figs. 17(a) and 17(b), respectively (solid lines). Appreciable differences can be observed even for indices of j as high as 10. Note that for values of θ_1 higher than about 90°, the values of R_j and y_j are generally lower than the asymptotic values of R_∞ and y_∞. As mentioned above, it can be seen that these differences decrease as j increases faster for y_j than for R_j.

7.2. Comparison with experiments

To evaluate the proposed model, the pictures on the left of Fig. 19 show a comparison between its results for R_j and measurements made on columns manufactured under different conditions with the experimental apparatus described in Section 6. Two sets of theoretical results are presented in Fig. 19, each for a different way of obtaining the values of θ_j for $j > 1$ used in the proposed model: a constant value of $\theta_j = \theta_d$ obtained from the average of the measured values represented by ■ symbols in Fig. 14, and a non-constant value of θ_j obtained from the fitted curve represented by a continuous line in Fig. 14. The two upper plots present the results obtained with paraffin droplets deposited on an AISI plate and a PVC plate, and the bottom plot presents the results obtained with Field's alloy droplets on an AISI plate. The experimental results are average values obtained from a series of about five manufactured columns (the vertical error intervals indicate the maximum and minimum values measured in each series). The figure shows a good degree of agreement between the experimental and theoretical results, which is slightly better when the values of θ_j obtained from the fitted curves in Fig. 14 are used in the model. Note that the radius of the sphere fitted to the deposited droplet for the paraffin columns decreases as j increases, reaching the asymptotic value R_∞ for values of j greater than around 4. Note also that this trend is different for metallic columns, for which $\theta_1 > 90°$ and the asymptotic value is reached almost from the second droplet deposited. Therefore, the differences between the proposed model and the one proposed by Gao and Sonin [1] are expected to be smaller for columns manufactured with metal droplets than with paraffin droplets.

To further show the improvements achieved with the proposed model in predicting the geometry of manufactured columns under real operating conditions, the pictures on the right of Fig. 19 compare the measured lengths L_n with the values predicted by the proposed model and by the model proposed in [1]. Note that the maximum total length of a column would be $2nR_{in}$ for the ideal case with $\theta_1 = \theta_j = 180°$. The figure shows a relatively good degree of agreement between the experimental and theoretical results, except for the values predicted with the model proposed in [1] when the columns are manufactured with paraffin, which show a

Table 5
Data considered for the manufacture of Sn63/Pb37 vertical interconnects.

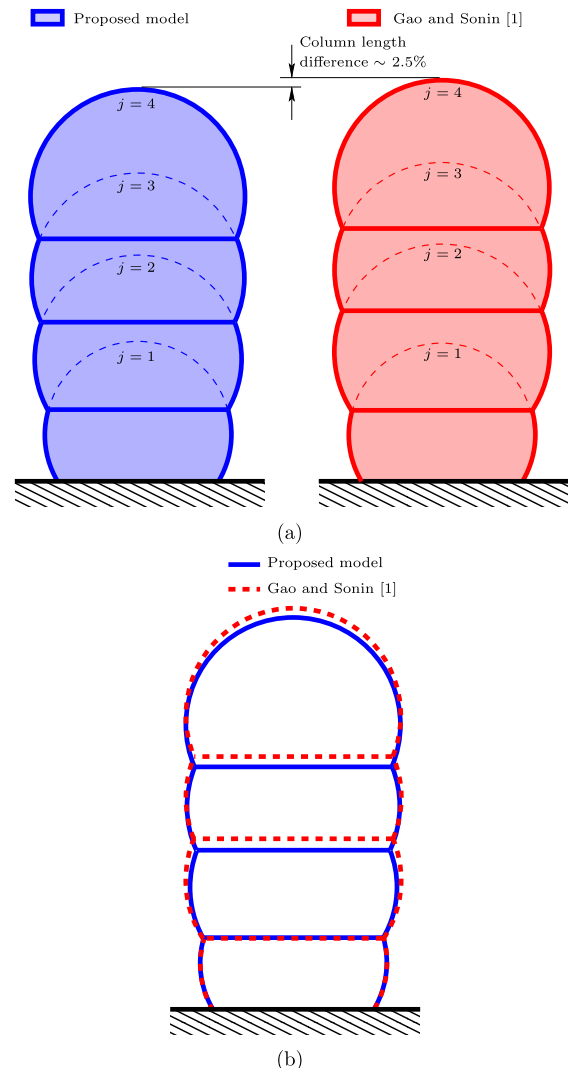|	
Incoming droplet radius, R_{in} (μm)	25
Number of droplets, n	4
Contact angle θ_1 (°)	120
Contact angle θ_d (°) ($\theta_j = \theta_d$ for $j > 1$)	45

(a)

(b)

Fig. 21. Vertical interconnector manufactured under the conditions of Table 5. (a) Comparison between the results predicted by the proposed model (picture on the left) and the model proposed in [1] (picture on the right). (b) Comparison between the two models, showing only the visible contours of the columns.
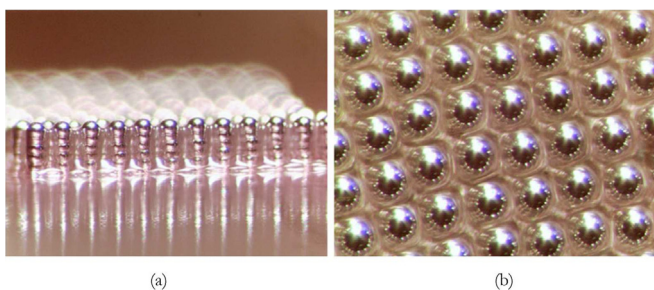

(a)   (b)

Fig. 20. Photographs, courtesy of Microfab Technologies, Inc., of a polymer filled Sn63/Pb37 solder column array for a chip-scale, wafer-level packaging concept. (a) Side and (b) top views.

significant deviation from the experimental data. Therefore, for wide ranges of contact angles the model proposed in [1] does not correctly predict the geometry of structures manufactured by drop-on-drop deposition, for which the model proposed in this work should be used.

7.3. Example of industrial interest

Obviously, inaccuracies in the geometric estimation of manufactured structures can make it difficult to automate the manufacturing process. It is expected that the increased accuracy achieved with the model proposed in this work will also improve process

planning. As an example of industrial interest that highlights the advantages of the proposed model, we consider below the printing of high aspect ratio vertical solder columns, which are used to eliminate failures associated with thermal expansion mismatch between integrated circuits and circuit boards in chip-scale packaging applications [36] (see Fig. 20).

A vertical interconnect manufactured by deposition of four Sn63/Pb37 droplets on a metallized circuit wafer will be considered. The size of the incoming droplets and contact angles assumed for this example, which can be considered as typical values in these applications, are shown in Table 5. The resulting theoretical radii of the deposited droplets are $R_1 = 26.46$ μm, and $R_j = 30.59$ μm
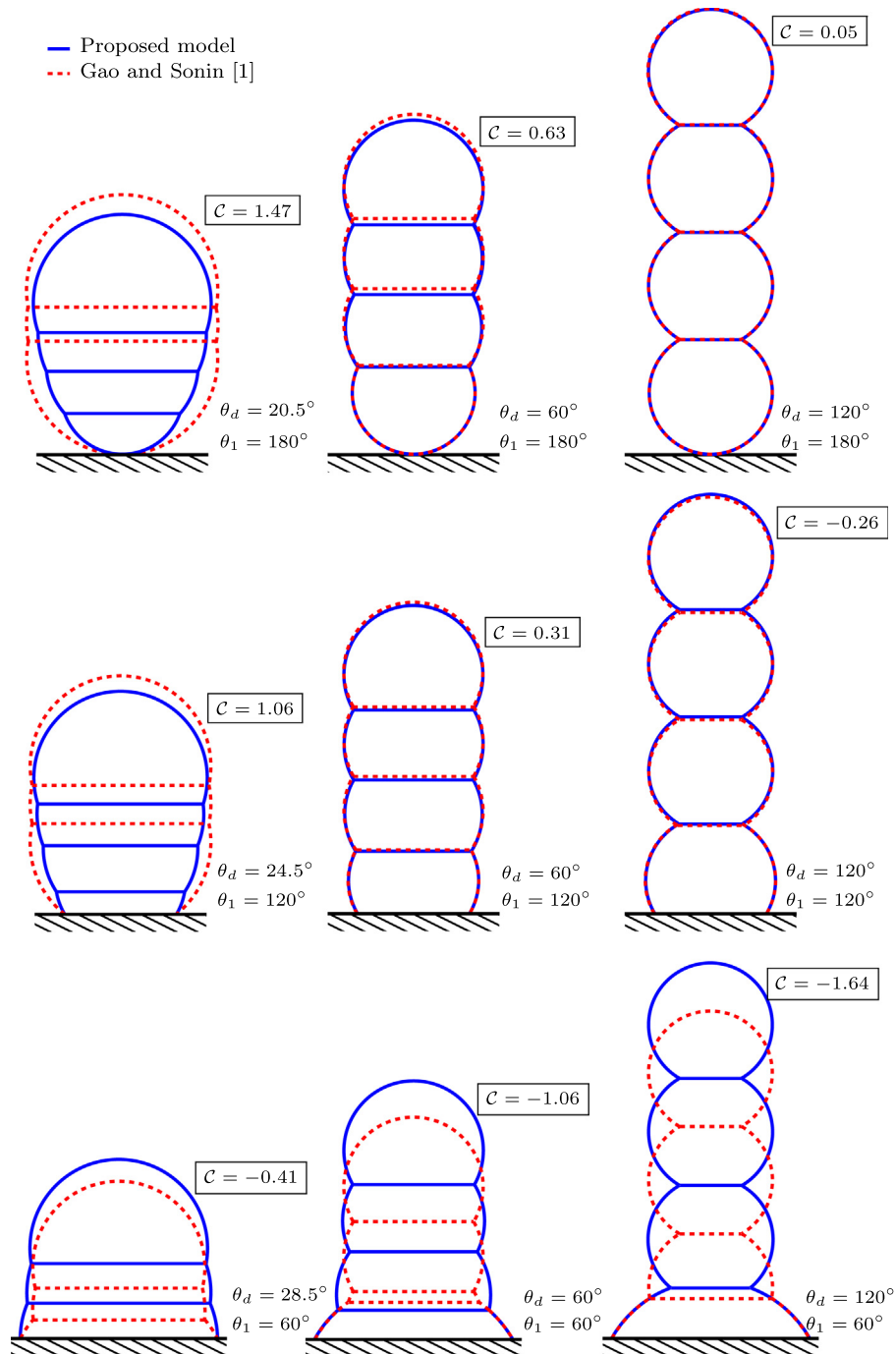

Fig. 22. Vertical interconnects manufactured under different conditions (nine combinations of θ_1 and θ_d values, with $\theta_j = \theta_d$ for $j > 1$). Comparison between the results predicted by the proposed model and that by Gao and Sonin [1]. Only the visible contours of each column are shown.

($j > 1$) when using the model by Gao and Sonin [1] and $R_2 = 29.37 \ \mu m, R_3 = 30.23 \ \mu m$, and $R_4 = 30.48 \ \mu m$ when using the proposed model. The length of the manufactured column equals $L_4 = 114.05 \ \mu m$ when using the model proposed in [1] and $L_4 = 111.29 \ \mu m$ when using the proposed model, which represents an appreciable difference of 2.5%. Fig. 21 shows the interconnect geometries predicted by the proposed model and the model proposed in [1]. The differences between both models are clearly visible. The volume-conservation parameter $\mathscr{C}$ of Eq. (15) turns out to be equal to 0.6 and the volume error of the model proposed in [1] is 5.5% of the total volume of the deposited material.

Fig. 22 shows the predictions of the proposed model and the model proposed in [1] for the geometry of columns manufactured by four-droplet deposition for different contact angles. The images on the left are obtained for the values of θ_j corresponding to the limiting cases defined by Eq. (17) (first two images on the top) or Eq. (18) (bottom image). The corresponding values of $\mathscr{C}$ are indicated in each picture. Note that for some conditions the differences between both models are substantial and that the parameter $\mathscr{C}$ can be considered a good indicator of the similarity between them (as $|\mathscr{C}|$ increases the similarity decreases). Note also that $\mathscr{C}$ is positive when the column volume predicted by the Gao&Sonin model is larger than the exact deposited volume and negative otherwise.

The results presented in this section confirm the importance of an accurate estimation of the final geometry of structures manufactured by dropwise deposition. It has been shown that the Gao&Sonin model can produce poor predictions for typical operating conditions, making it difficult to automate and control the manufacturing process. It is expected that this difficulty will be reduced by the improvement achieved with the proposed model to accurately predict the final shape of the manufactured structures.

8. Conclusions

An improved analytical model has been proposed to accurately determine the geometry of structures manufactured by molten drop-on-drop deposition under dropwise conditions. The model, which preserves exactly the volume of the deposited material and matches the solidification contact angle between consecutive deposited droplets, has been validated with experimental results obtained using different materials for the droplets and substrate. A good degree of agreement has been obtained between the experiments and the results obtained with the proposed model. It has been shown that the proposed model represents a great improvement over the well-known Gao&Sonin model for the estimation of the geometry of manufactured structures under dropwise operating conditions, which could represent an important step forward and be of great use in process planning and manufacturing automation.

Data availability

The raw/processed data required to reproduce these findings cannot be shared at this time due to technical and time limitations.

Declaration of Competing Interest

The authors declare that they have no known competing financial interests or personal relationships that could have appeared to influence the work reported in this paper.

Acknowledgements

References

[1] F. Gao, A.A. Sonin, Precise deposition of molten microdrops: The physics of digital microfabrication, P. Roy. Soc. A-Math. Phy. 444 (1994) 533–554, https://doi.org/10.1098/rspa.1994.0037.

[2] U. Gebhardt, T. Gustmann, L. Giebeler, F. Hirsch, J.K. Hufenbach, M. Kästner, Additively manufactured AlSi10Mg lattices - Potential and limits of modelling as-designed structures, Mater. Des. 220 (2022) 110796, https://doi.org/10.1016/j.matdes.2022.110796.

[3] P.-T. Lee, C.-H. Chang, C.-Y. Lee, Y.-S. Wu, C.-H. Yang, C.-E. Ho, High-speed electrodeposition for Cu pillar fabrication and Cu pillar adhesion to an Ajinomoto build-up film (ABF), Mater. Des. 206 (2021) 109830, https://doi.org/10.1016/j.matdes.2021.109830.

[4] K. Imaizumi, A. Fujita, A. Suzuki, M. Kobashi, K. Ozaki, Novel approach in fabricating microchannel-structured La(Fe, Si)13Hy magnetic refrigerant via low-contamination route using dissolutive mold, Mater. Des. 217 (2022) 110651, https://doi.org/10.1016/j.matdes.2022.110651.

[5] S.Z. Chavoshi, S. Goel, P. Morantz, Current trends and future of sequential micro-machining processes on a single machine tool, Mater. Des. 127 (2017) 37–53, https://doi.org/10.1016/j.matdes.2017.04.057.

[6] K. Liu, H. Wu, R. Huang, N.Y.J. Tan, Ultra-precision machining of micro-step pillar array using a straight-edge milling tool, Nanomanuf. Metrol. 3 (2020) 260–268, https://doi.org/10.1007/s41871-020-00076-1.

[7] T.Y. Ansell, Current status of liquid metal printing, J. Manuf. Mater. Process. 5 (2021) 31, https://doi.org/10.3390/jmmp5020031.

[8] D. Hayes, D. Wallace, Solder jet printing: Wafer bumping and csp applications, Chip Scale Review 2 (1998) 75–80.

[9] D.J. Hayes, D.B. Wallace, M.T. Boldman, R.M. Marusak, Picoliter solder droplet dispensing, Int. J. Microcircuits Electr. Packaging 16 (1992) 173–180.

[10] Y. Chao, A novel selection method of slice thickness in metal micro-droplet deposition manufacture, J. Manuf. Process. 21 (2016) 153–159, https://doi.org/10.1016/j.jmapro.2015.12.003.

[11] Z. Luo, X. Wang, L. Wang, D. Sun, Z. Li, Drop-on-demand electromagnetic printing of metallic droplets, Mater. Lett. 188 (2017) 184–187, https://doi.org/10.1016/j.matlet.2016.11.021.

[12] N. Gilani, N.T. Aboulkhair, M. Simonelli, M. East, I. Ashcroft, R.J.M. Hague, Insights into drop-on-demand metal additive manufacturing through an integrated experimental and computational study, Addit. Manuf. 48 (2021) 102402, https://doi.org/10.1016/j.addma.2021.102402.

[13] A. Da Silva, J. Frostevarg, J. Volpp, A.F.H. Kaplan, Additive Manufacturing by laser-assisted drop deposition from a metal wire, Mater. Des. 209 (2021) 109987, https://doi.org/10.1016/j.matdes.2021.109987.

[14] M. Simonelli, N. Aboulkhair, M. Rasa, M. East, C. Tuck, R. Wildman, O. Salomons, R. Hague, Towards digital metal additive manufacturing via high-temperature drop-on-demand jetting, Addit. Manuf. 30 (2019) 100930, https://doi.org/10.1016/j.addma.2019.100930.

[15] J. Vaithilingam, E. Saleh, L. Körner, R.D. Wildman, R.J.M. Hague, R.K. Leach, C.J. Tuck, 3-Dimensional inkjet printing of macro structures from silver nanoparticles, Mater. Des. 139 (2018) 81–88, https://doi.org/10.1016/j.matdes.2017.10.070.

[16] K. Abernathy, Future trends in digital design and additive manufacturing, Santa Fe Symposium on Jewelry Manufacturing Technology (2016) 1–22.

[17] A. Kalkal, S. Kumar, P. Kumar, R. Pradhan, M. Willander, G. Packirisamy, S. Kumar, B.D. Malhotra, Recent advances in 3D printing technologies for wearable (bio)sensors, Addit. Manuf. 46 (2021) 102088, https://doi.org/10.1016/j.addma.2021.102088.

[18] K.A. Kravanja, M. Finšgar, A review of techniques for the application of bioactive coatings on metal-based implants to achieve controlled release of active ingredients, Mater. Des. 217 (2022) 110653, https://doi.org/10.1016/j.matdes.2022.110653.

[19] M.S. Saleh, C. Hu, R. Panat, Three-dimensional microarchited materials and devices using nanoparticle assembly by pointwise spatial printing, Sci. Adv. 3 (2017) e1601986, https://doi.org/10.1126/sciadv.1601986.

[20] D.B. Wallace, D.J. Hayes, Solder jet printing of micropads and vertical interconnects, Proceedings, SMTA's Emerging Technology Symposium, Minneapolis, Minn. (1997). http://www.microfab.com/images/papers/smta97.pdf.

[21] Y. Chao, L. Qi, Y. Xiao, J. Luo, J. Zhou, Manufacturing of micro thin-walled metal parts by micro-droplet deposition, J. Mater. Process. Technol. 212 (2012) 484–491, https://doi.org/10.1016/j.jmatprotec.2011.10.015.

[22] M. Fang, S. Chandra, C.B. Park, Experiments on remelting and solidification of molten metal droplets deposited in vertical columns, J. Manuf. Sci. E.T. ASME 128 (2007) 311–318, https://doi.org/10.1115/1.2540630.

[23] M. Fang, S. Chandra, C. Park, Heat transfer during deposition of molten aluminum alloy droplets to build vertical columns, J. Heat Trans-T. ASME 131 (2009) 112101, https://doi.org/10.1115/1.3156782.

[24] C.-H. Wang, H.-L. Tsai, Y.-C. Wu, W.-S. Hwang, Investigation of molten metal droplet deposition and solidification for 3d printing techniques, J. Micromech.

Microeng. 26 (2016) 095012, https://doi.org/10.1088/0960-1317/26/9/095012.

[25] J. Che, S. Ceccio, G. Tryggvason, Computations of structures formed by the solidification of impinging molten metal drops, Appl. Math. Model. 28 (2004) 127–144, https://doi.org/10.1016/S0307-904X(03)00122-7.

[26] S. Haferl, D. Poulikakos, Experimental investigation of the transient impact fluid dynamics and solidification of a molten microdroplet pile-up, Int. J. Heat Mass Tran. 46 (2003) 535–550, https://doi.org/10.1016/S0017-9310(02)00289-2.

[27] S. Haferl, D. Poulikakos, Transport and solidification phenomena in molten microdroplet pileup, J. Appl. Phys. 92 (2002) 1675–1689, https://doi.org/10.1063/1.1492019.

[28] M. Liu, H. Yi, H. Cao, R. Huang, L. Jia, Heat accumulation effect in metal droplet-based 3D printing: evolution mechanism and elimination strategy, Addit. Manuf. 48 (2021) 102413, https://doi.org/10.1016/j.addma.2021.102413.

[29] D. Zhang, L. Qi, J. Luo, H. Yi, X. Hou, Direct fabrication of unsupported inclined aluminum pillars based on uniform micro droplets deposition, Int. J. Mach. Tool. Manu. 116 (2017) 18–24, https://doi.org/10.1016/j.ijmachtools.2017.01.001.

[30] D. Zhang, L. Qi, J. Luo, H. Yi, W. Xiong, Y. Mo, Parametric mapping of linear deposition morphology in uniform metal droplet deposition technique, J. Mater. Process. Tech. 264 (2019) 234–239, https://doi.org/10.1016/j.jmatprotec.2018.08.048.

[31] R. Bhola, S. Chandra, Parameters controlling solidification of molten wax droplets falling on a solid surface, J. Mater. Sci. 34 (1999) 4883–4894, https://doi.org/10.1023/A:1004680315199.

[32] R. Zamora, J. Hernández Ortega, J. López, F. Faura, J. Hernández, Development of a facility for molten metal micro-droplets generation. Application to microfabrication by deposition, Procedia Eng. 132 (2015) 110–117, https://doi.org/10.1016/j.proeng.2015.12.486.

[33] W. Wu, L. Chow, C. Wang, M. Su, J. Kizito, Jet impingement heat transfer using a Field's alloy nanoparticle - HFE7100 slurry, Int. J. Heat Mass Transf. 68 (2014) 357–365, https://doi.org/10.1016/j.ijheatmasstransfer.2013.09.029.

[34] W. Rasband, 2016. ImageJ software v1.51d. U.S. National Institutes of Health - NIH, Maryland.

[35] T. Loulou, E.A. Artyukhin, J.P. Bardon, Estimation of thermal contact resistance during the first stages of metal solidification process: II - experimental setup and results, Int. J. Heat Mass Transf. 42 (1999) 2129–2142, https://doi.org/10.1016/S0017-9310(98)00338-X.

[36] D. Wallace, D. Hayes, T. Chen, V. Shah, D. Radulescu, P. Cooley, K. Wachtler, A. Nallani, Ink-jet as a MEMS manufacturing tool, in: First International Conference on Integration and Commercialization of Micro and Nanosystems, Parts A and B. (2007) 1161–1168, https://doi.org/10.1115/MNC2007-21051.